Orientation-dependent properties of nanoparticle impact

Christian Schöner and Thorsten Pöschel*
Institute for Multiscale Simulations, Friedrich-Alexander-Universität Erlangen-Nürnberg, D-91052 Erlangen, Germany

(Received 15 April 2018; published 8 August 2018)

The mechanical properties of nanoparticles cannot be reliably described by bulk material characteristics due to their atomic structure, leading to pronounced anisotropic behavior. By means of molecular dynamics simulations, we study the impact of 5-nm Ag particles on an adhesive rigid wall. We show that the main characteristics of the impact such as the coefficient of normal restitution, the sticking probability, the maximal contact force, and the degree of plastic deformation of the particle depend sensitively on the angular orientation of the nanoparticle prior to the impact. We introduce the scalar parameter Ω describing the orientation and show that the impact characteristics can be described as functions of Ω.

DOI: 10.1103/PhysRevE.98.022902

I. INTRODUCTION

The contact of nanoparticles with surfaces is a key aspect to several technical processes such as comminution, filtration, agglomeration, etc. Therefore, the contact of nanoparticles is the subject of intensive research (for recent reviews see, e.g., [1,2]). Despite intensive research, the available model descriptions are still insufficient to reliably characterize the process of a nanoparticle impacting a solid plane.

Macroscopic contact models such as the (dissipative) Hertzian contact force [3,4] or the Johnson-Kendall-Roberts (JKR) model [5,6] consider the particle as homogeneous and isotropic. While this approximation is well justified for ordinary granular particles, for nanoparticles it fails for two reasons: (i) Nanoparticles consisting of a few thousand atoms only cannot be considered isotropic due to their atomic structure, and (ii) the surface to volume ratio of nanoparticles is large, such that their mechanical behavior is determined not only by bulk properties but also to a large extent by surface effects. The size effect of the mechanical properties was quantified, e.g., in [7]. By means of molecular dynamics (MD) simulations it is shown that the effective Young's modulus of metal particles of size 30–40 nm agree with the macroscopic bulk value up to 1%; however, for smaller particles, the deviation increases to about 30% for 2-nm particles.

An important characteristic describing the dissipative collision of particles is the coefficient of normal restitution, that is, the ratio of the normal components of the rebound velocity and the impact velocity. While for larger particles, the coefficient of restitution can be derived from bulk properties by integrating Newton's equation [8,9] this concept fails for nanoparticles when the molecular or crystal structure of the material becomes apparent [10]. A striking example was provided by Kuninaka and Hayakawa [11], who investigated thermal rebound, where thermal energy of colliding particles may be transferred into kinetic energy, leading to large fluctuations of the coefficient of restitution, including in rare cases values exceeding unity, from which one could erroneously conclude a violation of the second law, valid for *thermodynamic* systems.

Given non-negligible influence of (attractive) surface forces, colliding nanoparticles may stick to one another, similar to adhesive granular particles [12], that is, the coefficient of restitution drops to zero. By analyzing the reassignment of kinetic energy into other degrees of freedom upon impact, it was found that the minimal sticking probability coincides with an impact velocity where no energy exchange mode is dominating [13]. These very general findings are investigated in more depth in terms of a plastic deformation analysis in [14], where a fcc-hcp transition is observed. This transition can be reversible or irreversible, but causes dissipation through heating in both cases. While for macroscopic bodies the loss of mechanical energy quantified by the coefficient of restitution is due to local deformation in the contact zone, (see, e.g., [4]), such a local description is not sufficient for nanosized crystalline particles. Here, for large enough impact velocity, dissipative deformations are not restricted to the contact region but nonlocal plane gliding of the particle material is observed. The interplay of these different deformation modes leads to scaling relations for the coefficient of restitution [15] different from what is known from macroscopic theory [4]. For macroscopic bodies other than single crystals or other exceptionally well ordered materials, due to inhomogeneities of the material, plane gliding is much less important, which may be considered as a major difference of the physics of collisions of granular particles as compared to nanoparticles. Obviously, crystallographic plane gliding depends strongly on the orientation of the impacting particles, which was, however, not investigated in [15], where only a single orientation of the particle was considered.

From the theory of crystals, it is well known that many physical properties of a crystalline material depend on the angular orientation such as Young's modulus, the specific electric resistance, the speed of sound, the rate of solution, and others, where the amount of anisotropy depends on the material (see, e.g., [16]). This anisotropy affects, of course, also the impact mechanics of nanoparticles. While this fact is generally acknowledged, currently there is virtually no

*thorsten.poeschel@fau.de

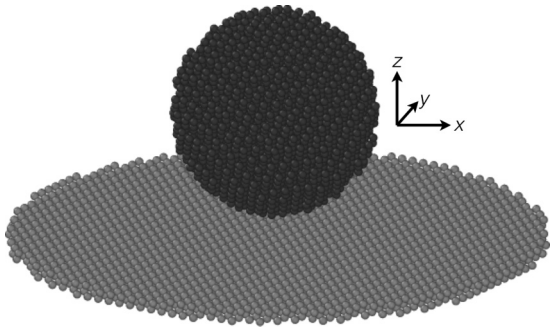

FIG. 1. Initial state of the system nanoparticle-wall.

systematic investigation of anisotropy effects of impacts of nanoparticles beyond [17], where the impact of extremely small particles with McKay icosahedra geometry was considered. For such particles, three characteristic orientations are identified, leading to different impact behaviors. However, the particles considered are extremely small such that there is no bulk phase present, that is, practically all atoms belong to the surface. Consequently, the impact properties are mainly determined by the shape of the surface patch that gets in touch with another object at impact.

Recently, Millán *et al.* [18,19] studied the critical velocity for elastic-plastic transition of nanoparticle impacts. Their work succeeds in finding a dislocation-emission based model that is able to describe their simulation results. In their case, averaging over 1000 random orientations prior to the impact was performed to obtain orientation-independent averaged data.

In the present paper, we study systematically the anisotropy of the impact mechanics of a silver particle of diameter 5 nm with an adhesive rigid wall by means of molecular dynamics simulations. The precollisional structure of the particle is described by a fcc lattice. Depending on the orientation of the particle, the process of impact is determined by both surface shape effects and volume effects, corresponding to plane gliding of the crystal structure. We present a characteristic measure to describe the orientation dependency and show that it characterizes the impact properties in a certain velocity range more adequate than the largest Schmid factor, which is considered the dominant crystallographic parameter in shear mechanics. For smaller impact rate, surface shape dominates the impact properties.

II. NUMERICAL SIMULATION METHOD

A. Interaction models and system geometry

We investigate the collision of a nanoparticle with a solid adhesive wall by means of molecular dynamics. It was shown that MD simulations of low-pressure impaction deliver reliable results for the coefficient of restitution [20], well in agreement with experiments. The initial state is sketched in Fig. 1.

The nanoparticle and the plane are both cut out from a fcc grid. The wall is modeled as an ideally stiff cylindrical [100]-terminated fcc grid, that is, the atoms of the wall are located at fixed positions (no significant differences could be found when using the [111]-terminated plane instead). The diameter of the flat cylinder is chosen to be six times the radius of the impacting particle. Its height is three layers of atoms (see Fig. 1). We checked that the size of the cylinder is large enough such that boundary effects due to the finite size of the target are not noticeable for all sets of parameters used. The nearest neighbor distance of the grid is the distance at which the Lennard-Jones potential, Eq. (2), vanishes.

For the interaction between the atoms the particle consists of, we assume an embedded atom model (EAM) [21]. The energy of atom i is given by

$$E_i^{\mathrm{EAM}} = F\left(\sum_{j\neq i}\rho(r_{ij})\right) + \frac{1}{2}\sum_{j\neq i}\phi(r_{ij}), \tag{1}$$

where F is the embedding energy functional, ρ is the atomic electron density function, and ϕ is a pair interaction potential as a function of the distance, r_{ij}, of the atoms. This model is reliable in reproducing material properties of bulk crystals like the sublimation energy and the elastic constants (see [22]). For the simulation, we use the material parameters for silver provided in [22]. For the interaction between wall atoms and particle atoms we applied a cutoff and smoothed Lennard-Jones-Potential

$$E_i^{\mathrm{LJ}} = 4\epsilon\sum_{j\neq i}\left(\frac{\sigma}{r_{ij}}\right)^{12} - C\left(\frac{\sigma}{r_{ij}}\right)^{6} + C_1 r_{ij} + C_2, \tag{2}$$

where $\epsilon = 5.521\times10^{-20}$ J, $\sigma = 2.644$ Å, and $C = 0.35$ are the depth of the energy well, the characteristic Lennard-Jones distance, and a dimensionless parameter modeling a weakly adhesive contact, based on the assumption of a partial oxide layer weakening the interaction [23]. The constants C_1 and C_2 are chosen to ensure smooth transition at the cutoff distance $r_c = 2.5\,\sigma$.

B. Preparation of the initial state

The equations of motion due to Eqs. (1) and (2) are integrated using the MD code LAMMPS [24] with time step 6×10^{-16} s. Initially, the spherical nanoparticle of diameter 5 nm cut out from a fcc grid was placed such that a unit cell is centered at the origin and the orientation of the grid coincides with the orientation of the target plane. Using the parameters of silver [22], the nanoparticle comprises 3513 atoms.

The particle was equilibrated at temperature 300 K using a Nosé-Hoover thermostat and then the nanoparticle was simulated as a microcanonical ensemble for 20 000 time steps, in order to obtain a stable equilibrium state. The equilibrated particle was placed just outside of the Lennard-Jones interaction range of the wall in the positive z direction (see Fig. 1). After thermal equilibration the desired impact velocity in the range $v_i \in [10,\ 400]$ m/s was subtracted from the z component of each atom the particle consists of, that is, the particle impacts the plane at v_i with the atoms fluctuating due to thermal noise.

The main part of the scatter of the results presented below results from the relative position of the lattices of the wall and the particle. Therefore, for each simulation of impact, the particle is randomly shifted in the direction of the target by up to one lattice period in both directions, x and y. Thus averaging over the lattice structure of the target was achieved by 1000

repetitions of the simulation at random shift. The scatter due to the initial temperature of the particle was significantly smaller than the scatter due to the shift of the lattices. The influence of temperature is not systematically studied here.

Finally, in order to study the effect of anisotropy of the nanoparticle that is the focus of the current paper, we rotate the nanoparticle with respect to a rotation axis and a certain angle. This procedure will be explained in detail in the next section.

C. Initial orientation of the particle and the parameter Ω

To investigate the orientation dependency, we determined 1000 uniformly distributed random rotations of the particle with respect to the wall. Considering the embedding sphere of the cluster, the aim of this rotation is to assure that (a) each point of the sphere is located at the south pole with equal probability, that is, when the particle moves in the negative z direction each point has the same probability to touch the target plane first, and (b) the angle between the orientations of the lattices of the target material and the particle is equally distributed. Such a transformation is achieved using the method by Miles [25], where a rotation axis is determined by the center of the sphere embedding the particle and a randomly chosen point on its surface [26]. The particle is then rotated around this axis by the random angle α with probability density

$$p(\alpha) = \frac{2}{\pi}\sin^2\frac{\alpha}{2}, \quad \alpha \in [0, \pi]. \tag{3}$$

In the following, the orientations are characterized by the orientation parameter Ω which arises from the coordinate transformation of the load direction from reference into the crystal coordinate system (see Fig. 2):

$$\Omega(\gamma_1, \gamma_2, \gamma_3) \equiv \gamma_1^2\gamma_2^2 + \gamma_2^2\gamma_3^2 + \gamma_3^2\gamma_1^2 \tag{4}$$

$$= (\cos^2\phi \sin^2\phi - 1)\sin^4\theta + \sin^2\theta. \tag{5}$$

In Eq. (4), γ_i are the direction cosines from the coordinate transformation, and ϕ and θ are the axes of the spherical coordinate system (see Fig. 2).

Before describing the properties of Ω, let us discuss the symmetry of the problem: The projection of a cubic unit cell onto the the unit sphere delivers 48 spherical triangles as can be seen from Fig. 3 (left). These triangles are equivalent due to the symmetry of the fcc structure [see Fig. 3 (right)].

Therefore, Ω is completely determined on the whole sphere by its values on the spherical triangle bound by the points $(0, 0, 1)$, $(1, 0, 1)/\sqrt{2}$, $(1, 1, 1)/\sqrt{3}$, which we call the *critical triangle* in agreement with the literature, e.g. [16] [see Fig. 3 (left)].

D. The probability measure P_Ω

To obtain the cumulative probability distribution, $P_\Omega(\Omega)$, which will be used to analyze the properties of the impact with respect to the orientation of the particle, we calculate the integrals $P_\Omega(\Omega < x)$, $0 \leqslant x \leqslant \frac{1}{3}$ exploiting the symmetry of the fcc structure, that is, by reducing the problem to the calculation of the distribution on the critical triangle.

On the critical triangle, Ω depends strictly monotonously on θ and ϕ with $\Omega((0, 0, 1)) = 0$, $\Omega((1, 0, 1)/\sqrt{2}) = 1/4$, and $\Omega((1, 1, 1)/\sqrt{3}) = 1/3$ (see Fig. 4). For convenience of integration, we divide the critical triangle into the areas (i) and (ii) separated by the isoline $\Omega = 1/4$ (see the dashed line in Fig. 4).

(i) $0 \leqslant \Omega \leqslant \frac{1}{4}$.

(ii) $\frac{1}{4} < \Omega \leqslant \frac{1}{3}$.

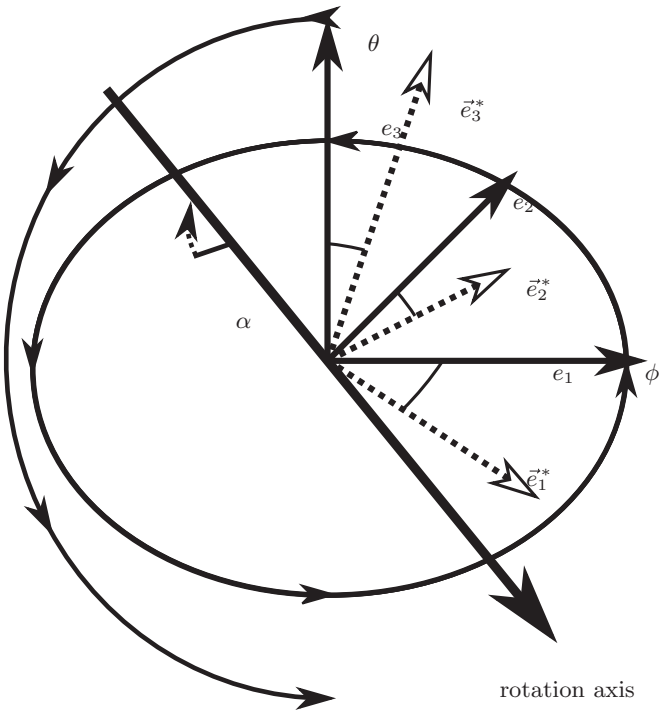

FIG. 2. Definition of the polar and azimuthal spherical coordinate system angles, θ and ϕ (curved line arrows), and the canonical standard coordinate system vectors, $\vec{e}_1 \equiv (1, 0, 0)$, $\vec{e}_2 \equiv (0, 1, 0)$, $\vec{e}_3 \equiv (0, 0, 1)$. By application of the orthogonal rotation given by the random rotation axis and the angle α, it is transformed into the coordinate system $\{\vec{e}_1^*, \vec{e}_2^*, \vec{e}_3^*\}$. The direction cosines used in Eq. (4) are given by $\gamma_i \equiv \vec{e}_i \cdot \vec{e}_i^*$.

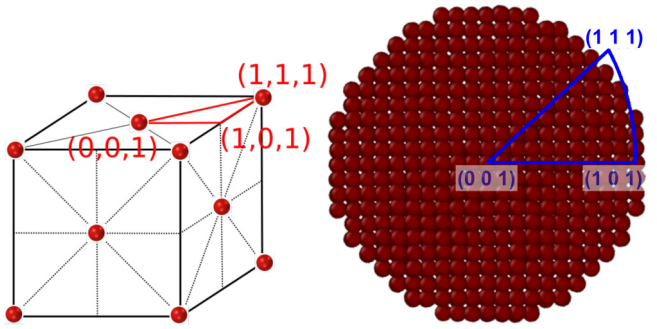

FIG. 3. Definition of the *critical triangle*. Left: The projection of the cubic unit cell onto the unit sphere delivers 48 spherical triangles. Right: Layer of atoms located at the center of the particle in initial (nonrotated) position with the critical triangle superimposed (blue). Due to the symmetry of the FCC structure, all 48 spherical triangles are equivalent.

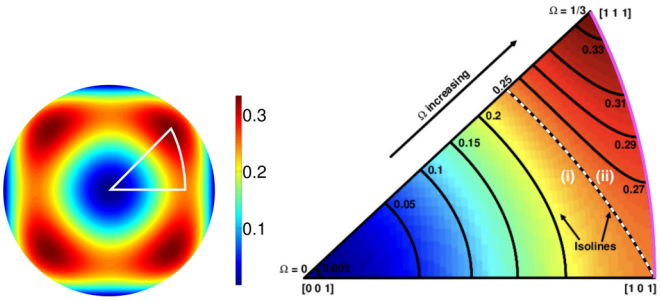

FIG. 4. Left: The function $\Omega(\phi,\theta)$ on the unit sphere. The position of the critical triangle is indicated. Right: On the critical triangle, Ω is a strictly monotonous function of θ and ϕ. For the computation of the probability distribution, $P_\Omega(\Omega)$, we divide the critical triangle into the areas (i) and (ii), separated by the isoline $\Omega = 1/4$ (dashed line). The pink line shows the big arc used for the computation of the distribution function for area (ii) [Eq. (11), see the text for explanation].

The integration domain due to area (i) can be characterized as limited by $0 \leqslant \phi \leqslant \pi/4$ and $0 \leqslant \theta \leqslant \tilde{\theta}$, where $\tilde{\theta}$ is a function of Ω and ϕ. This function is obtained by solving Eq. (5) for θ with respect to Ω and ϕ in this critical triangle:

$$\tilde{\theta}(\Omega,\phi) = \arcsin\sqrt{\frac{-1+\sqrt{1+4\Omega(\mathrm{cs}^2\phi-1)}}{2(\mathrm{cs}^2\phi-1)}}, \tag{6}$$

with $\mathrm{cs}^2\phi \equiv \cos^2\phi\sin^2\phi$. The tilda in Eq. (6) indicates that this solution is restricted to the critical triangle. Using the identity $\cos[\arcsin(x)] = \sqrt{1-x^2}$ and taking into account that the area of one triangle is $\frac{4\pi}{48}$, we obtain inside area (i)

$$\begin{aligned} P_\Omega\left(\Omega \leqslant \frac{1}{4}\right) &= \frac{48}{4\pi}\int_0^{\frac{\pi}{4}}\int_0^{\tilde{\theta}(\Omega,\phi)} \sin(\theta)\,d\theta\,d\phi \\ &= \frac{12}{\pi}\int_0^{\frac{\pi}{4}}\left[1-\sqrt{1-\frac{-1+\sqrt{1+4\Omega(\mathrm{cs}^2\phi-1)}}{2(\mathrm{cs}^2\phi-1)}}\right]d\phi. \end{aligned} \tag{7}$$

The boundaries of the integrals corresponding to area (ii) are more complicated since here the boundary with respect to ϕ depends on Ω. This third side of the triangle is part of the big arc containing $(1,0,1)/\sqrt{2}$ and $(1,1,1)/\sqrt{3}$ [see the pink line in Fig. 4 (right)]. Therefore, a normal vector to it is given by $(1,0,-1)$, concluding $x = z$ on this side of the triangle. Now let θ^* and ϕ^* be the restrictions of the spherical coordinates to this boundary to area (ii). Then

$$\cos(\phi^*)\sin(\theta^*) = \cos(\theta^*), \tag{8}$$

$$\theta^*(\phi) = \operatorname{arccot}[\cos(\phi^*)]. \tag{9}$$

Inserting Eq. (9) into Eq. (5) and rearranging delivers the boundary of area (ii) [pink line in Fig. 4 (right)] as a pure function of Ω:

$$\phi^*(\Omega) = \arccos\sqrt{\frac{1-\Omega+\sqrt{1-3\Omega}}{1+\Omega}}. \tag{10}$$

Consequently, the limits of area (ii) are given by $\phi^*(\Omega) \leqslant \phi \leqslant \frac{\pi}{4}$ and $\tilde{\theta}(\Omega = \frac{1}{4},\phi) \leqslant \theta \leqslant \tilde{\theta}(\Omega,\phi)$. For the computation of the remaining part of the distribution function [area (ii)] we exploit the above-denoted formula for $P(\Omega = \frac{1}{4})$, and write

$$\begin{aligned} P_\Omega\left(\Omega > \frac{1}{4}\right) &= P_\Omega\left(\Omega = \frac{1}{4}\right) + \frac{12}{\pi}\int_{\phi^*(\Omega)}^{\frac{\pi}{4}}\int_{\tilde{\theta}(\frac{1}{4},\phi)}^{\tilde{\theta}(\Omega,\phi)} \sin(\theta)\,d\theta\,d\phi \\ &= P_\Omega\left(\Omega = \frac{1}{4}\right) + \frac{12}{\pi}\int_{\phi^*}^{\frac{\pi}{4}}\left[\sqrt{\frac{2\mathrm{cs}(\phi)+1}{2(\mathrm{cs}(\phi)+1)}} - \sqrt{1-\frac{-1+\sqrt{1+4\Omega(\mathrm{cs}^2\phi-1)}}{2(\mathrm{cs}^2\phi-1)}}\right]d\phi. \end{aligned} \tag{11}$$

The derivatives of the integrals in Eqs. (7) and (11) can be calculated analytically (using MAPLE or another symbolic formula manipulation tool) to yield the probability density, $p_\Omega(\Omega)$. Since this expression is rather cumbersome, for convenient practical application we provide a fit to the ansatz:

$$p_\Omega^{\mathrm{fit}}(\Omega) = a\ln\left|\Omega-\tfrac{1}{4}\right| + b\,\Omega + c, \tag{12}$$

where a, b, and c are real numbers for both sides of the singularity at $\Omega = \frac{1}{4}$:

$$p_\Omega^{\mathrm{fit}}(\Omega) = \begin{cases} -1.402\,\ln\left(\frac{1}{4}-\Omega\right) - 2.493\,\Omega - 0.4388 & \text{for } \Omega < \frac{1}{4} \\ -1.328\,\ln\left(\Omega-\frac{1}{4}\right) + 2.989\,\Omega - 1.287 & \text{for } \Omega > \frac{1}{4} \end{cases}. \tag{13}$$

Integrating $p_\Omega^{\mathrm{fit}}(\Omega)$ delivers handy equations for $P_\Omega^{\mathrm{fit}}(\Omega)$:

$$P_\Omega^{\mathrm{fit}}(\Omega) = \begin{cases} \Omega(0.9632-1.2465\Omega) + 1.402\left(\frac{1}{4}-\Omega\right)\ln\left(\frac{1}{4}-\Omega\right) + 0.4859 & \text{for } \Omega \leqslant \frac{1}{4} \\ \left(\Omega-\frac{1}{4}\right)\left[1.4945\left(\Omega-\frac{1}{4}\right) - 1.328\ln\left(\Omega-\frac{1}{4}\right) + 0.78825\right] + 0.6489 & \text{for } \Omega > \frac{1}{4} \end{cases}. \tag{14}$$

We point out that this fit is universal for the probability density of Ω for a randomly rotated particle impacting the plane. It is independent of any material properties but only restricted to the fcc lattice structure. The quality of the fit can

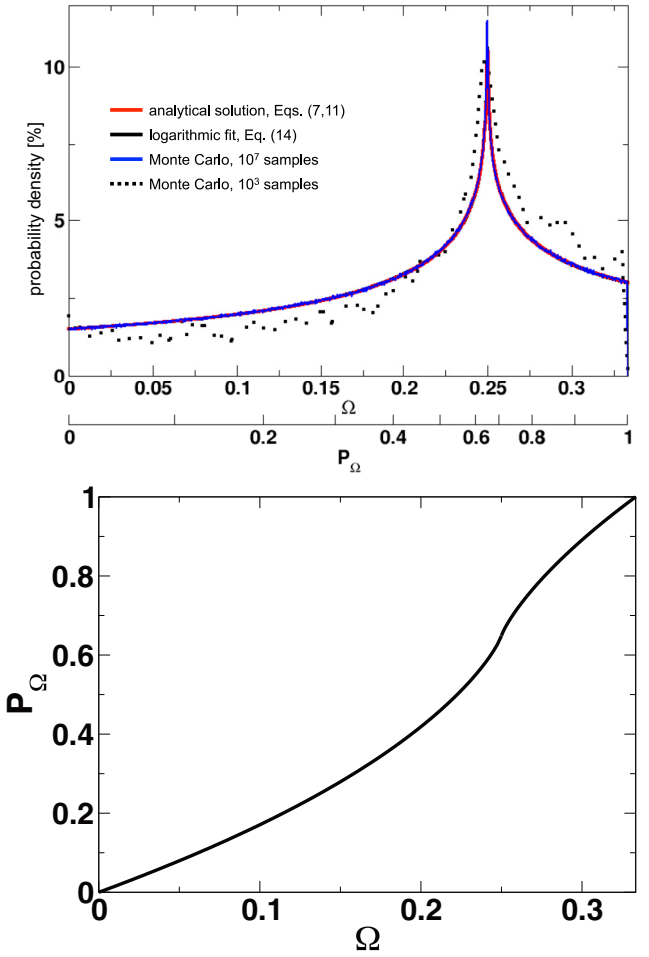

FIG. 5. Top: Probability density, $p_\Omega(\Omega)$, of a randomly rotated particle. The figure shows the analytical solution, Eq. (11), the logarithmic fit, Eq. (13), and the results of a Monte Carlo sampling (in extension of the 1000 random orientations, a total of 10^7 random orientations were determined to check coincidence with the other curves). The simulation data set coincides up to good agreement with the other datasets. The analytical solution, Eq. (11), the fit, Eq. (14), and the MC sampling coincide even up to linewidth. Bottom: Corresponding cumulative probability, $P_\Omega(\Omega)$. The function $P_\Omega(\Omega)$ is used to draw the second horizontal axis in the top figure.

be assessed in Fig. 5 (top) showing the analytical solution for the probability density $p_\Omega(\Omega)$, according to Eq. (11) together with the fit given in Eq. (13) and the results of a Monte Carlo sampling. The coefficient of determination (R^2 value) of the fit is $R^2 \geqslant 0.999$ for both parts with 10^7 uniformly distributed sampling points in $[\delta, \frac{1}{4} - \delta]$ and $[\frac{1}{4} + \delta, \frac{1}{3} - \delta]$. The value $\delta = 10^{-6}$ is needed to deal with the discontinuity of the density such that near the pole about 6×10^{-6} of the total range of Ω remains unsampled, which is good enough for all practical considerations. The curves are plotted together with the values obtained for the 1000 random orientations of the particle shown in Fig. 5. The bottom panel of Fig. 5 shows the cumulative probability distribution, $P_\Omega(\Omega)$, according to Eqs. (7) and (11) which we will use in the subsequent text.

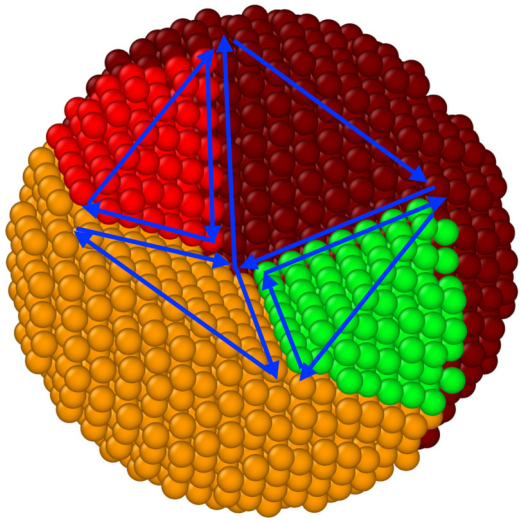

FIG. 6. Slip planes and slip directions of the FCC structure inside of a particle. The four colors distinguish the different stacks of FCC slip planes.

III. SIMULATIONS OF NANOPARTICLE IMPACT

A. Characteristics of inelastic interaction

We investigated the impact of a particle of random orientation and position as described above. In particular, we consider four characteristics of inelastic collisions, that is, dissipative interaction: (1) the amount of plastic deformation; (2) the maximal contact force, $F_{\max}$; (3) the coefficient of normal restitution, e_n; and (4) the sticking probability, p_s. All of these characteristics of the crystalline particle are intimately related to plane gliding. Figure 6 shows the four slip planes and corresponding three directions to each slip plane, amounting to a total of 12 slip directions. The four colors belong to the different layers of slip planes. The sensitivity of a crystalline particle against sliding due to stress in a certain direction is characterized by the Schmid factor [16]: According to Schmid's law, the critical resolved shear stress, τ, relates to total stress, σ, applied to a material in a certain direction via $\tau = \sigma m = \sigma \cos\varphi \cos\vartheta$ where φ is the angle of the stress, σ, with the glide plane and ϑ is the angle of the stress, σ, with the glide direction. The Schmid factors are then defined as $2\cos\varphi\cos\vartheta$ with the corresponding values of φ and ϑ. As the Schmid factors, especially the largest and second largest, are key parameters to characterize plastic deformation of crystalline materials under stress, in many places we will refer to these numbers. We will show, however, that for the description of the impact dynamics of nanoscale particles Ω is more significant than the largest Schmid factor.

B. Plastic deformation

We quantify the plastic deformation of a particle due to an impact by the number of atoms which change their neighborhood relations. The neighborhood of an atom is defined by the set of other atoms located in a sphere of radius=1.5× (nearest neighbor distance of the lattice), and the neighborhood of an

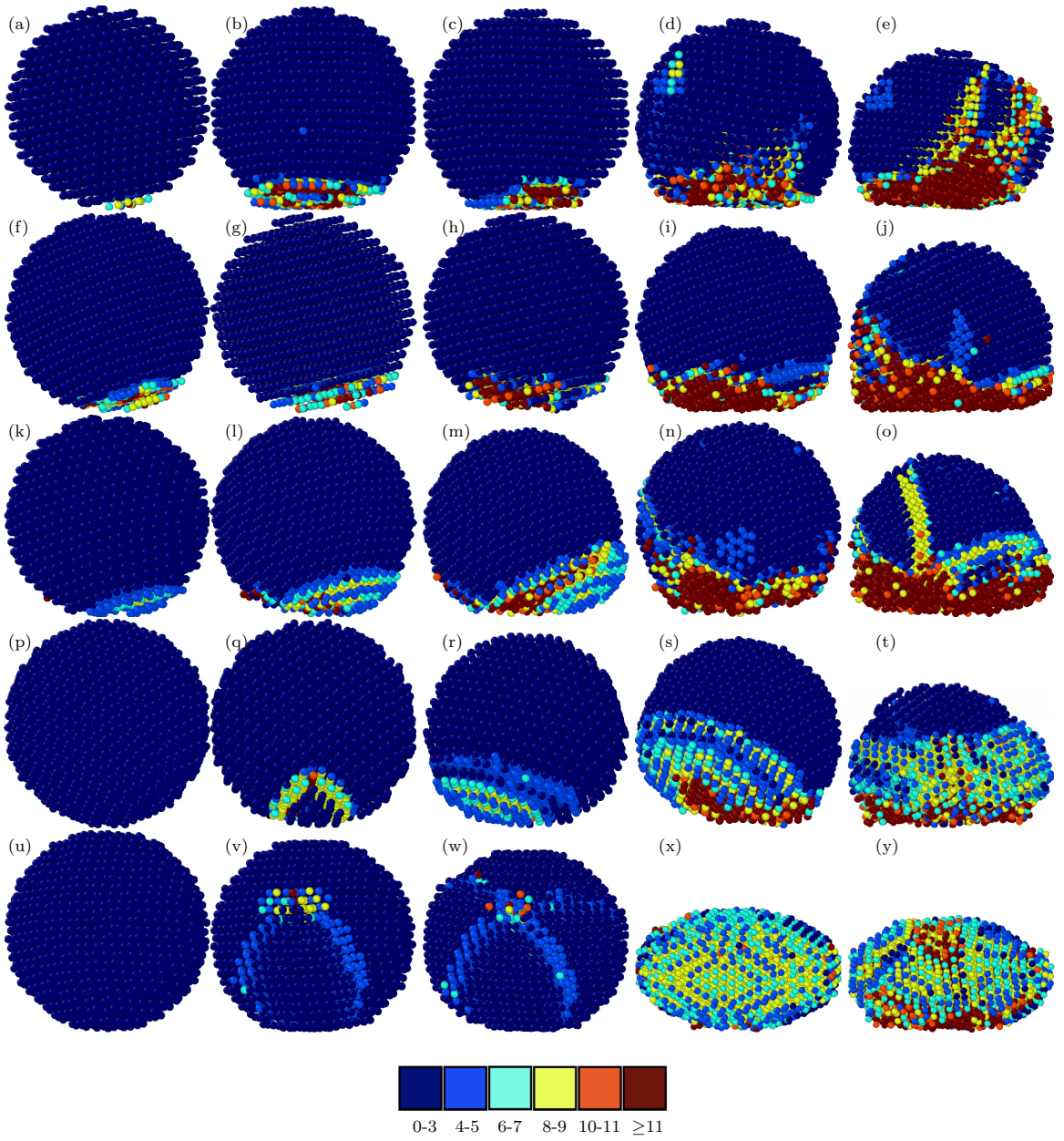

FIG. 7. The degree of plastic deformation of a particle impacting a plane in perpendicular direction depends on the impact velocity, v_i, and the relative orientation of the lattice structures of the particle and the plane. The figure shows examples of particles impacting the plane at $v_\mathrm{i} = (40,\ 100,\ 150,\ 300,\ 400)\,\mathrm{m/s}$ (columns from left to right) and at angular orientation characterized by $P_\Omega = 1, 0.75, 0.5, 0.25, 0$ (rows from top to bottom). The images show the particles at the instant of maximal compression when the center of mass velocity changes its direction. The number of changed neighbors of the atoms is coded by color. The labels (a)–(y) refer to the marks in Figs. 8, 10, 12, and 13.

atom are called changed if the set of neighbors before the impact differs from the set after the impact. Because of the finite temperature of the impacting particle there is a certain thermal noise in the neighborhood, concerning in particular the atoms close to the surface the total binding energy of which is low. The average amount of atoms which change their neighborhood due to thermal motion amounts to approximately 3 for the parameters used. Figure 7 shows typical examples of particles at the instant of maximal compression when the center of mass velocity changes its direction. Rows in Fig. 7 correspond to the same impact velocity, v_i; columns correspond to the same value of P_Ω characterizing the angular orientation. The degree of plastic deformation is coded by color.

Figure 8 shows the plastic deformation as a function of the impact velocity v_i and the orientation measure, P_Ω. The data points are sampled with increments of $\Delta v_\mathrm{i} = 10\,\mathrm{m/s}$ and $\Delta P_\Omega = 0.025$. For each data point, $(v_\mathrm{i},\ P_\Omega)$, we averaged over 1000 impacts at different orientations all characterized by the same values of v_i and P_Ω.

As expected, the degree of plastic deformation increases with increasing impact velocity. From the plot Fig. 8 (bottom), which is averaged with respect to velocity, we see that for

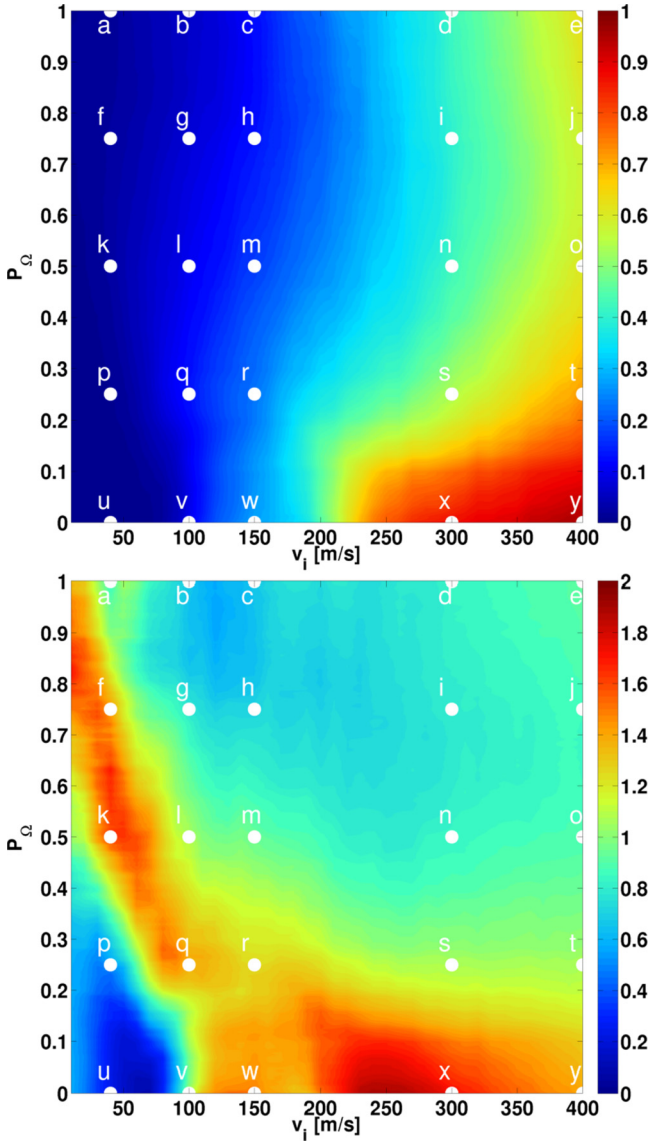

FIG. 8. Top: Plastic deformation as a function of the impact velocity, v_i, and the orientation, P_Ω. Color codes for the fraction of atoms with changed neighborhood. Bottom: The same data but normalized for each velocity individually. The color indicates the plastic deformation (fraction of atoms with changed neighborhood) normalized by the plastic deformation at the given velocity but averaged over all orientations, Ω. The marks (a)–(y) refer to the labels in Fig. 7 showing a representative of an impact with the corresponding (v_i, Ω) combination. The labels (a)–(y) refer to the marks in Fig. 7.

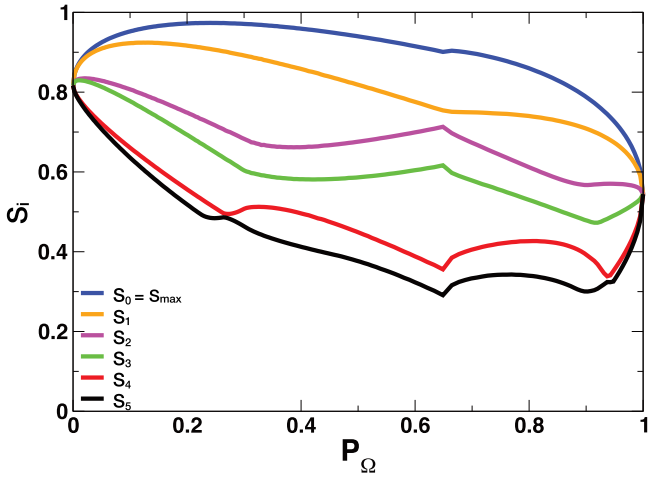

FIG. 9. Averaged values of the largest six Schmid factors $S_i(P_\Omega)$ with respect to P_Ω.

$v_i = 10\,\mathrm{m/s}$ the amount of plastic deformation is much higher for $P_\Omega > 0.5$ as compared to $P_\Omega < 0.5$. A band of high relative plastic deformation moves to lower values of P_Ω with increasing v_i until $v_i \approx 100\,\mathrm{m/s}$. This can be understood from the fact that the particle surface is not perfectly spherical due to its crystalline structure: In the [1,1,1] direction, corresponding to $P_\Omega = 1$ ($\Omega = 0.\overline{3}$), and the [0,0,1] direction, corresponding to $P_\Omega = 0$ ($\Omega = 0$) (see Fig. 4), the surface of the particle is terminated by very small portions of crystal planes. For $P_\Omega = 1$, the three outermost layers contain 12, 61, and 102 atoms and are of maximal planar density. In contrast, for $P_\Omega = 0$, the three outermost layers contain 32, 69, and 88 atoms, and the layers are of submaximal packing density. At low impact velocities, plastic deformation develops in the form of irreversible plane gliding, that is, shearing of the outermost layers, since atoms located in these layers have only one neighboring crystal layer. Since plane gliding happens only in planes of maximal planar density, the amount of plastic deformation is bigger for $P_\Omega > 0.5$ as compared with the orientations $P_\Omega < 0.5$. Consequently, as can be seen from Fig. 9, the largest Schmid factor is always larger than 0.8; therefore, for the cases $P_\Omega < 0.5$, the plane gliding is reversible and happens more on the inside of the particle (see Fig. 7 bottom left images).

As velocity increases, the force due to the impact causes plastic deformation also for orientations corresponding to smaller P_Ω. The mentioned band structure comes from the fact that the shear angle for the outermost layer is equal to zero for $P_\Omega = 1$ and increases for orientations with smaller values of P_Ω such that the average number of the dislocated atoms increases with v_i due to increased impact energy and, thus, the number of dislocated atoms with larger P_Ω decreases relative to the average.

For $v_i < 100\,\mathrm{m/s}$, the lowest values of P_Ω show almost no plastic deformation (see Fig. 8). For these orientations, the stress due to impact leads only to reversible plane gliding but not to plastic, persistent deformation. At $v_i \approx 100\,\mathrm{m/s}$, we observe a transition of irreversible plane gliding due to increased impact energy, leading to persistent changes of the neighborhood for many atoms simultaneously. Essentially, two cases can be distinguished: Either a single dislocation travels through the entire particle on a certain slip direction, and hits the other boundary of the particle, or two dislocations hit each other to also generate a persistent stacking fault (see Fig. 8). At this point, surface effects or close-to-surface effects become unimportant regardless of the orientation, since the number of atoms changing their neighbors due to irreversible plane gliding dominates.

The behavior at larger impact velocity can be understood from the discussion of the Schmid factors characterizing the

sensitivity of a crystalline particle against sliding due to stress in a certain direction (see Sec. III A). For slow forcing and given orientation, the largest Schmid factor determines whether slip occurs, where a minimum of 45° between impact plane and crystal layer is required classically. Since Ω describes the orientation of the crystalline structure of the particle with respect to the target, obviously, the maximal Schmid factor $S_{\max}$ and Ω must be related (see Fig. 9). The relation between $S_{\max}$ and Ω is not a mathematical function since several orientations Ω belong to the same value of $S_{\max}$ and vice versa. Such a relation exists only for the sum of all Schmid factors of the FCC lattice:

$$\Omega = \frac{1}{2} - \frac{3}{8}\sum_i S_i^2. \tag{15}$$

Nevertheless, Fig. 9 shows that the six largest Schmid factors grow from $P_\Omega = 1$ to 0, except for some intervals where the S_i are nearly constant and some rather short intervals where they even decrease. Thus, as a rule of thumb, small values of Ω correspond to *good slip systems*, that is, only small deformation due to compression is required to activate a second, third, or fourth slip plane. Therefore, for orientations corresponding to large values of P_Ω, stress is released by shear of the outermost layers, that exhibit quite weak slip systems, but only one layer is neighboring, weakening the cohesive attraction. This effect is of microscopic nature and cannot be observed for macroscopic impaction which is implied by weak adhesion and very high volume to surface ration. While the maximum Schmid factor characterizes slip for slow (quasistatic) deformation, it is not entirely adequate for stress due to impact at high velocity as the dynamics is due to shocks and other nonequilibrium effects. As a consequence not only is the slip plane corresponding to the maximum Schmid factor activated but also other slip planes related to other Schmid factors (in particular the second largest) become activated. Moreover, close to the contact zone, atoms leave their fcc lattice positions and are densified. This process consumes a lot of energy and thereby the total amount of atoms getting plastically deformed depends less on v_i as compared to smaller values of P_Ω.

Starting from $v_\mathrm{i} \approx 200\,\mathrm{m/s}$, this effect becomes dominant for the lowest 15% of P_Ω, where many slip planes are activated, causing plastic shear deformation additionally to the irreversible plane gliding. Eventually at $v_\mathrm{i} = 300\,\mathrm{m/s}$, almost all atoms are involved in plastic deformation for this part of the distribution. As velocity is further increased, the impact energy becomes so large that most of the fcc structure is converted upon impact. This deformation causes local transformations of the crystal structure leading to mostly bcc structure, corresponding to larger values of free energy and a more compact and, thus, pressure resistant unit cell.

Before discussing the main macroscopic characteristics of the impact, the maximal contact force, $F_{\max}$, the coefficient of restitution, e_n, and the sticking probability, p_s, quantitatively in dependence on the orientation of the impact, we wish to recall the significance of Ω: Obviously, the unique description of the orientation of the particle needs two parameters, θ and ϕ (see Fig. 2). However, as we show here, certain combinations of θ and ϕ lead to the same macroscopic behavior of the impact, characterized by $F_{\max}$, e_n, and p_s. It turns out that

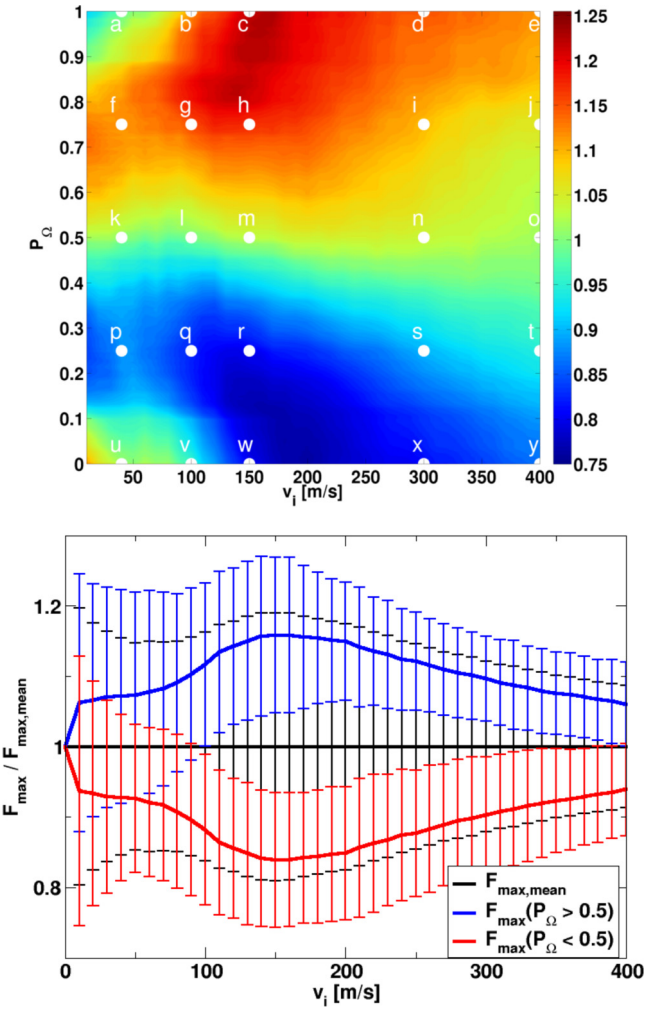

FIG. 10. Top: Maximal contact force, $F_{\max}(v_\mathrm{i}, P_\Omega)$, normalized with respect to velocity. The labels (a)–(y) refer to the marks in Fig. 7. Bottom, blue curve: Normalized maximal force, $\langle F_{\max}\rangle_{P_\Omega \geqslant 0.5}(v_i)/\langle F_{\max}\rangle_{P_\Omega}(v_i)$ where $\langle F_{\max}\rangle_{P_\Omega \geqslant 0.5}(v_i)$ stands for the average over all impacts at v_i and orientations with $P_\Omega \geqslant 0.5$ and $\langle F_{\max}\rangle_{P_\Omega}(v_i)$ stands for the average over all impacts at v_i and all orientations, P_Ω. Red curve: Same for $P_\Omega < 0.5$. Vertical lines are error bars indicating the standard deviations. The color of the error bars correspond to the average data of the same color. Black curve and error bars correspond to all orientations. Here, the average is identical unity, of course.

the two-dimensional manifold, (θ, ϕ), may be expressed by a one-dimensional manifold, Ω. That is, impacts characterized by the same value of Ω reveal the same characteristics, despite the fact that they correspond to different combinations (θ, ϕ). The reason for this mapping is the fact that not θ and ϕ directly but the Schmid factors (in particular the two largest ones) are responsible for the impact behavior, supported by Eq. (15), expressing Ω in terms of the Schmid factors.

C. Maximal contact force, $F_{\max}$

The maximal interaction force during a collision as a function of impact velocity, v_i, and orientation, P_Ω, is shown in Fig. 10. To understand this figure, we refer to Fig. 9: the

orientation $P_\Omega = 0$ represents active systems, corresponding to small contact force at impact. With increasing P_Ω, the particle appears more and more rigid since slip in the bulk of the particle relates to large loss of energy of the impact. Therefore, the contact force assumes its maximum for orientations corresponding to $P_\Omega = 1$ where plastic deformation dominates (see Fig. 10).

For $v_i \lesssim 100\,\mathrm{m/s}$, this general argument does not describe the orientation dependency of the interaction force completely, since specific details of the crystalline structure at the contact point have a significant influence: For $P_\Omega = 0$ up to about $P_\Omega \approx 0.15$, the two largest Schmid factors and, thus, stress transmission increase (see Fig. 9), explaining the island of high maximal contact force $F_{\max}(P_\Omega \lesssim 0.15, v_i \lesssim 100\,\mathrm{m/s})$. Correspondingly, the comparatively low value of $F_{\max}(P_\Omega \gtrsim 0.85, v_i \lesssim 100\,\mathrm{m/s})$ can be explained by the fact that the shear angle is close to zero for such orientations. Consequently, the impact leads to a transfer of linear momentum into angular momentum causing particle rotation (see Fig. 7 top left). These effects are less significant for larger impact rate and also for other values of P_Ω, corresponding to bigger shear angle and irreversible plane gliding (i.e., shearing of the outermost layers).

Starting at $v_i \approx 100\,\mathrm{m/s}$, plane gliding becomes dominant and, therefore, the properties of the slip system govern the impact behavior. For large shear stress, shear along a single plane corresponding to the largest Schmid factor is not sufficient to resolve all stress and, thus, other shear planes are activated corresponding to the second largest and further Schmid factors. Here, the pertinence of the here introduced parameter Ω characterizing the impact behavior becomes particularly obvious as the general rule of thumb stated at the beginning of this subsection applies: Decreasing $P_\Omega = 1$ to 0, the particles' resistance against volume shear and plane gliding decreases and so does the maximal contact force. For $v_i \approx 120$–$200\,\mathrm{m/s}$, the relative values for the contact force span from 75 to 125%, the largest observed interval.

When the impact velocity is further increased, dislocation emission can be observed for all orientations (see Fig. 7 right columns). Additionally, we notice flattening of the contact area regardless of the orientation, due to very large impact energy. In this region, thus, we observe a combination of compression and plastic shear. For such impact parameters, the variation of the relative contact force decreases. The description of the orientation by P_Ω allows us to subdivide the possible particle orientation into families of classes revealing similar behavior. For example, Fig. 10 (bottom) shows the maximal contact force as a function of the impact velocity, normalized by the average value for all orientations for impacts with the same velocity. Thus, the average normalized force assumes the value 1 for all velocities, by definition. If we plot the data separately for classes of orientations belonging to $P_\Omega < 0.5$ and $P_\Omega > 0.5$ (red and blue lines), we see that P_Ω indeed classifies the orientations in a meaningful way. This can be quantified by the standard deviations of the cases $P_\Omega < 0.5$ and $P_\Omega > 0.5$ which are much smaller than the standard deviation of the averaged data (black line).

After this detailed discussion, we can restate the arguments by means of the here introduced parameter Ω: The orientation $P_\Omega = 0$ stands for good slip systems corresponding to small contact force at impact. With increasing P_Ω the particle behaves more and more rigidly since slip in the volume of the particle becomes more and more unfeasible. Thus, maximum contact force is achieved for orientations corresponding to $P_\Omega = 1$ where plastic deformation dominates. The relevance of the parameter P_Ω can also be seen in the examples shown in Fig. 7. In conclusion, the introduction of Ω allows for a convenient one-parameter description of the impact behavior.

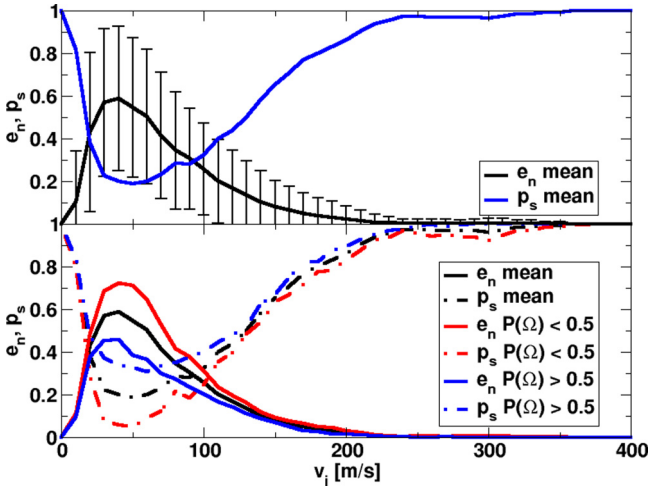

FIG. 11. Coefficient of normal restitution, e_n, and sticking probability, p_s, as functions of the impact velocity. Top: Expectation values of e_n and p_s averaged over all orientations and corresponding error bars. Bottom: Expectation values of e_n and p_s evaluated separately for arbitrary P_Ω (black lines), $P_\Omega \leqslant 0.5$ (red lines), and $P_\Omega \geqslant 0.5$ (blue lines). See the text for discussion.

D. Coefficient of restitution, e_n, and sticking probability, p_s

The coefficient of normal restitution, e_n, defined as the ratio of the normal components of the rebound velocity and the impact velocity, and the sticking probability, p_s, at which the rebound velocity drops to zero, are important global characteristics of a particle impacting a plane. Here we discuss the dependence of these parameters on the impact velocity and in particular on the orientation of the particle prior to impact, shown in Fig. 11. For small impact velocity up to about 100–200 m/s, the coefficient of restitution reveals large scatter indicated by large error bars (variance). This is again due to the crystalline structure of the particle and the variations of the slip properties in dependence on the orientation of the crystalline particle structure with respect to the target. Similar to the way in which this orientation characterized by the Schmid factors or Ω, respectively, has large effect on the interaction force discussed at length in Sec. III C, it affects also the global properties, e_n and p_s. This coincidence appears quite natural as the coefficient of restitution is a direct consequence of the interaction force; that is, given the interaction force as a function of impact velocity, the coefficient of restitution can be derived by integrating Newton's equation of motion. Examples for such analytical calculation for homogeneous (noncrystalline) materials have been done for viscoelastic spheres [8,9,27] and cylinders [28], simplified linear dashpot forces [29], and adhesive viscoelastic materials [12,30].

The coefficient of restitution as a function of the impact velocity, averaged over all angular orientation of the impacting

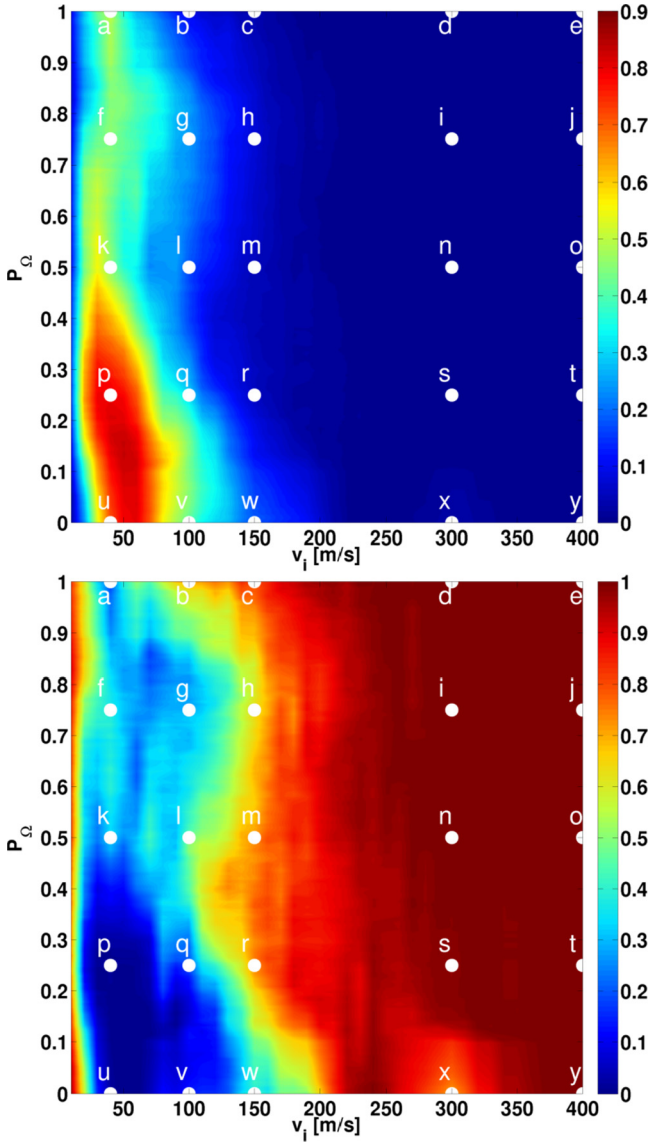

FIG. 12. Coefficient of normal restitution, e_n, and sticking probability, p_s (both indicated by color), as functions of the impact velocity, v_i, and the angular orientation, P_Ω. The labels (a)–(y) refer to the marks in Fig. 7. For discussion see the text.

particle as drawn in the upper part of Fig. 11, reveals large error bars indicating a variance of the same size as the data itself. Analyzing the data separately for $P_\Omega < 0.5$ and $P_\Omega > 0.5$ (bottom part), we obtain a clear separation of the data, that is, the average values for $P_\Omega < 0.5$ and for $P_\Omega > 0.5$ are well separated, indicating that P_Ω indeed groups families or angular orientations of similar behavior caused by the slip properties along different directions in the crystalline particle material. Figure 12 depicts this property of the Ω description in more detail. In the top panel, we can clearly see very different behavior for the families of orientation, $P_\Omega < 0.5$ and $P_\Omega > 0.5$, which is particularly prominent for small impact velocity, $v_i \lesssim 100\,\mathrm{m/s}$, in agreement with the integral presentation shown in Fig. 11 bottom. Obviously, at large impact velocity, $v_i \gtrsim 150\,\mathrm{m/s}$, a lot of irreversible, and thus dissipative, shear takes place at any orientation, leading to a small coefficient of restitution. In this velocity interval, the expectation values for $P_\Omega < 0.5$, $P_\Omega > 0.5$, and all values of P_Ω do not deviate much and the variance is small [see Fig. 11 (bottom), Fig. 13 (bottom left)].

The situation is different for small impact velocity, $v_i \lesssim 100\,\mathrm{m/s}$. Here the orientation of the particle prior to impact makes a significant difference. For small P_Ω, slip is active already for small stress (good slip system), thus much energy can be stored in reversible slip deformation during the impact. When the contact terminates, the particle relaxes and the elastically stored energy is retransformed into rebound velocity. Therefore, for small velocity and small P_Ω we find large values of the coefficient of restitution [see Fig. 12 (top)]. For large P_Ω we have a bad slip system, therefore the particle cannot elastically store a significant amount of energy. Instead, a large part of the kinetic energy of the impacting particles is dissipated due to plastic (nonreversible) deformation. Consequently, for small v_i and large P_Ω we obtain small values for the coefficient of restitution. The coefficient of restitution assumes its largest possible value $e_n \lesssim 1$ at $P_\Omega \approx 0.14$, where the largest Schmid factor attains its maximal value 1.0 (see Fig. 9).

The sticking probability, p_s, is closely related to the coefficient of restitution. It describes the situation that the impacting particle loses so much energy due to an impact that the postcollisional velocity is not sufficient to overcome the attractive adhesion force [see Eq. (2)], such that the coefficient of restitution drops to zero. Figure 12 (bottom) shows the sticking probability as a function of the impact velocity v_i and the orientation P_Ω. According to the close relation of p_s and e_n its behavior can be understood using exactly the same arguments as for the discussion of $e_n(v_i, P_\Omega)$ above.

Both p_s and e_n become special at *very* low impact rate, $v_i \lesssim 15\,\mathrm{m/s}$. In this range, the attractive part of the interaction force [Eq. (2)] causes the particle sticking to the surface, independently of the orientation. Even for perfectly elastic interaction corresponding to elastic slip, the energy of the postcollisional velocity would not be sufficient to overcome the attractive force. This effect can be seen in both panels of Fig. 12 in the form of a small vertical strip of nearly homogeneous color at the very left side.

An interesting feature can be seen in Fig. 12 (bottom) for $P_\Omega \lesssim 0.15$ and $v_i \approx 300\,\mathrm{m/s}$, close to the label (x): Here the sticking probability reveals a sharp increase. This effect is due to a *pancake flattening* [compare Fig. 7(x) against the neighboring subfigures, (r), (s), and (w)]. At this value of Ω four slip planes are activated simultaneously and the energy of the impacting particle is, thus, sufficient to cause a large (pancakelike) deformation. The behavior of the crystalline nanoparticle in this parameter region deviates strongly from the mechanics of a homogeneous, viscoelastic particle impacting a plane where sudden changes in the macroscopic behavior are not found.

E. Comparison of the significance of P_Ω and P_{SF} for the description of the orientation of the impacting particle

The Schmid factors are of fundamental importance for the description of materials subjected to shear stress. Of particular importance is the largest Schmid factor describing the onset of yield. In most places in the present paper, we characterize the impact of nanoparticles on a solid plane by

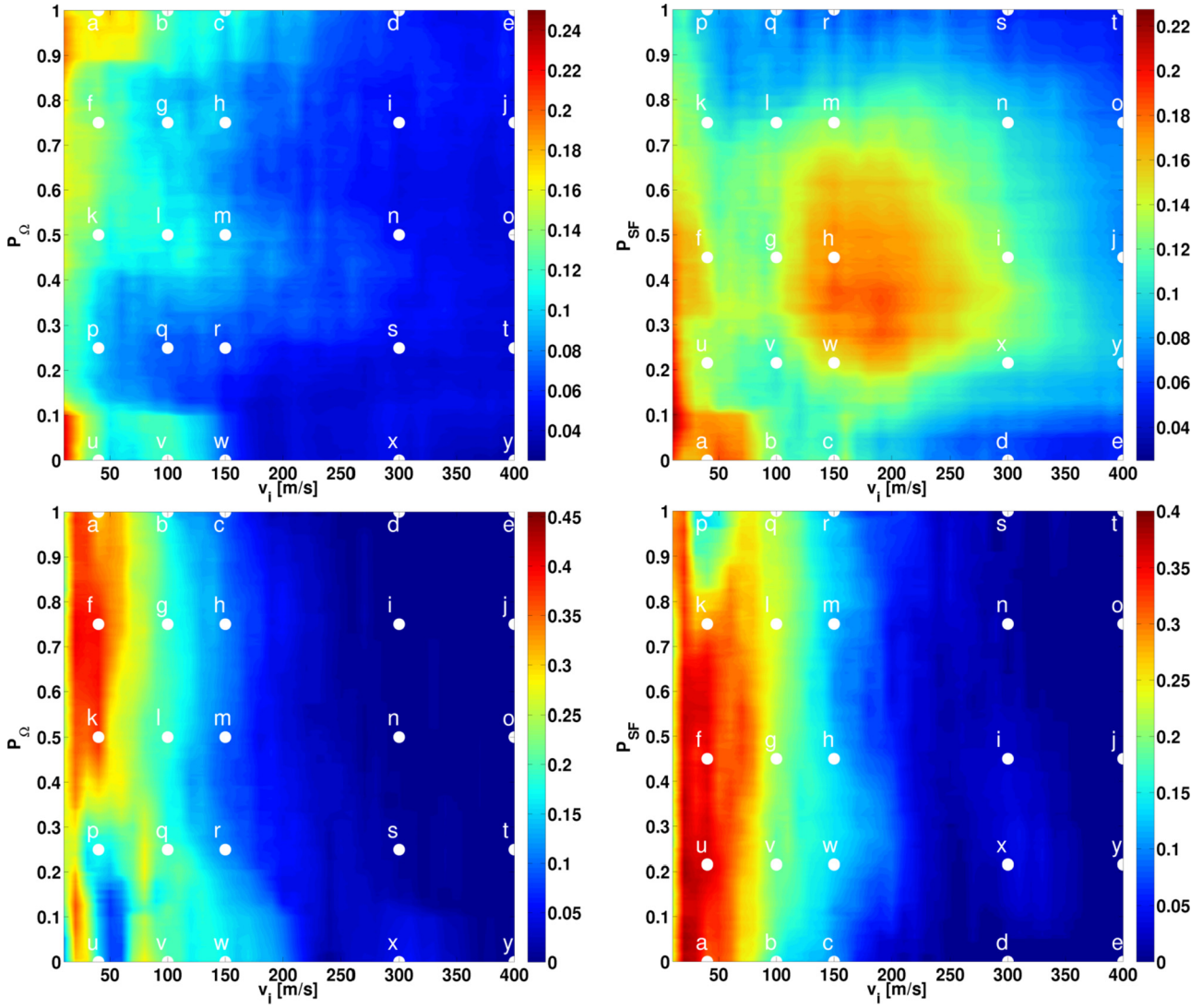

FIG. 13. Comparison of standard deviations for the description of the orientation by means of P_Ω (left figures) and P_{SF} (right figures). Top: $F_{\max}(v_{\mathrm{i}}, P_\Omega)$ and $F_{\max}(v_{\mathrm{i}}, P_{\mathrm{SF}})$, averaged with respect to velocity. Bottom: $e_{\mathrm{n}}(v_{\mathrm{i}}, P_\Omega)$ and $e_{\mathrm{n}}(v_{\mathrm{i}}, P_{\mathrm{SF}})$. Hereby, P_{SF} is constructed in a similar manner: $P_{\mathrm{SF}} \leqslant x$ corresponds to the area of the critical triangle with relative size $\frac{1}{x}$, where all Schmid factors lie below a certain value $P_{\mathrm{SF}}(S_{\max})$. The labels (a)–(y) refer to the marks in Fig. 7.

means of the parameter Ω, defined in Eq. (4), and its cumulative distribution, the measure P_Ω, defined in Eqs. (7) and (11). We employ additionally the two largest Schmid factors when necessary.

Obviously, the description by the full set of Schmid factors carries more information than the parameter Ω being a scalar value only. Nevertheless, we believe that for the problem considered in this paper the description by means of Ω is superior to the description by means of Schmid factors since it allows for a characterization of the impact orientation in an intuitive way. Obviously, a single parameter description is advantageous for a graphical representation of the system properties; more than one characteristic would require, at least, a four-dimensional representation. Thus, considering more than one orientation parameter for the plots makes them more difficult to understand and to interpret by a crystal-layer based understanding of the particle-wall impact system. It turns out that the extremal values of Ω together with the singular big arcs are clearly understandable in the sense of a layer model and also lead to distinct behavior, as the presented results show.

From a topological point of view, a consideration of the fcc crystal structure and a quasispherical outer boundary of the particle lead directly to the critical triangle (see Fig. 3). Thus, Ω is the simplest smooth function on the sphere that accounts for the underlying symmetry and exhibits extremal values at the geometrically most interesting points. But apart from providing a more intuitive representation, for the case of the impacting nanosphere, Ω indeed describes the orientation dependency better than the largest Schmid factor, $S_{\max}$, in the sense that accumulated standard deviations with respect to velocity of descriptions using Ω are smaller than those using P_{SF}. As an example, Fig. 13 shows the standard deviations of the maximal force, $F_{\max}$, as a function of the velocity and angular orientation of the impacting particle, drawn in (v_i, P_Ω)

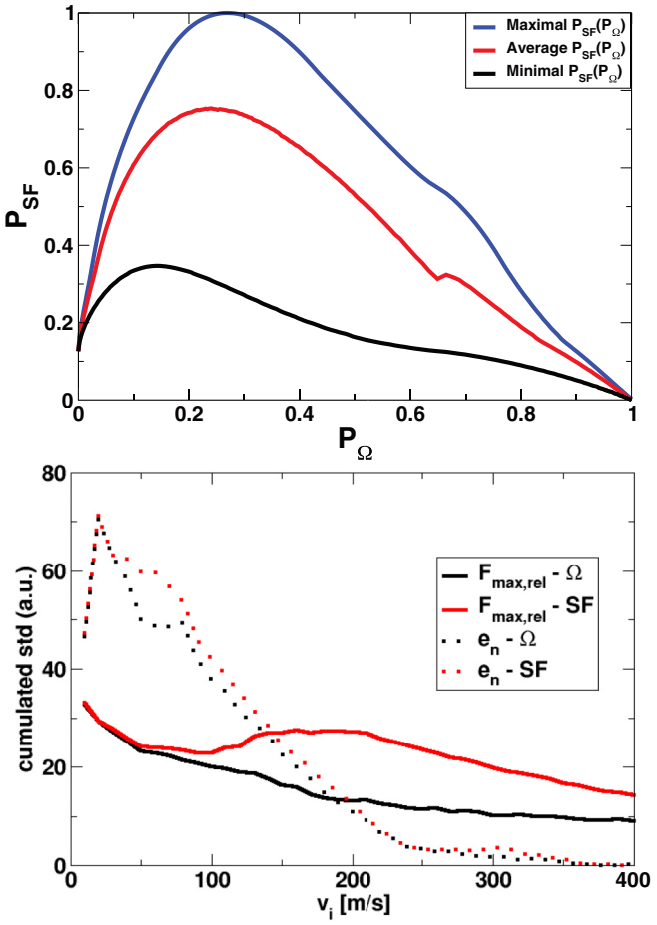

FIG. 14. Top: P_{SF} in relation to P_Ω. Bottom: Accumulated standard deviations of $F_{\mathrm{max}}^{\mathrm{rel}}(P_\Omega, v_i)$ and $e_n(v_i)$.

coordinates and (v_i, P_{SF}), respectively (top figures) and the same for the coefficient of normal restitution, e_n.

From Fig. 13 (top left and right) it can be seen that the description by P_{SF} exhibits large standard deviation in the inside of the image ($0.2 < P_{\mathrm{SF}} < 0.7$, $100\,\mathrm{m/s} < \mathrm{v_i} < 300\,\mathrm{m/s}$) as compared to P_Ω. So Ω possesses far better sensitivity for the investigation of F_{max} than S_{max} and its probability measure P_{SF}, respectively. In the description of the plot Fig. 13, the construction of P_{SF} is sketched. The further advantages of P_Ω over Ω should be clear now: We are able to compare percentages of all possible orientations.

The bottom plots in Fig. 13 show the standard deviations for the determination of e_n. Here, two things can be seen. First, for velocities below about 100 m/s, P_Ω exhibits a larger region of low standard deviation in the vicinity of the orientation $P_\Omega = 0.14$ with the largest observed coefficient of restitution e_n. Second, the localization of the pancake flattening within $P_\Omega < 0.15$ for $v_i \approx 300\,\mathrm{m/s}$ is much sharper as compared to $0.15 < P_{\mathrm{SF}} < 0.8$. For the relation between P_Ω and P_{SF}, see Fig. 14 (top). They are considerably different in the sense of that there is no one-to-one map between them. All together, Ω and P_Ω map the geometric positions on the critical triangle more cleverly to the intervals $[0, \frac{1}{3}]$ and [0,1], respectively.

Speaking quantitatively, Fig. 14 (bottom) shows the accumulated sums of the standard deviations with respect to velocity from Fig. 13. In the vicinity of the impact velocity, where e_n attains its maximal value, this sum is about 20% bigger for P_{SF}. For F_{max}, the sum for P_{SF} even doubles over the entire deformation driven impact regime $v_i \gtrsim 100\,\mathrm{m/s}$.

Concluding, P_Ω is better suited to describe the point of maximal e_n and the deformation driven impact regime $v_i > 100\,\mathrm{m/s}$ with respect to the maximal contact force during impact F_{max}, and able to observe the pancake flattening at around 300 m/s, where P_{SF} is not.

IV. CONCLUSION

For macroscopic spheres, the properties of impact with a wall or with one another are frequently characterized by the coefficient of restitution, ε. This description relies on two approximations, namely, the assumptions of instantaneous collisions and the homogeneity of the particle material. With appropriate description of the particle material, ε can be quantified. It turns out that ε is a function not only of the material characteristics but also of the impact rate. Such calculations have been done for realistic cases, e.g., for viscoelastic materials [8,9,27] and adhesive viscoelastic materials [12,30]. While the assumption of homogeneity certainly fails for nanoparticles due to the appearance of the atomar crystalline structure, qualitatively, their rebound resembles adhesive viscoelastic spheres: For small impact velocity, the energy of the postcollisional velocity is not sufficient to overcome adhesion. Therefore, the particle sticks to the surface, that is, $\varepsilon(0) = 0$. In the limit of large impact velocity, dissipative bulk deformations consume a large part of the precollisional kinetic energy, therefore $\lim_{v\to\infty} \varepsilon(v) = 0$. For moderate impact rate, the rebound of adhesive viscoelastic spheres resembles the rebound of nonadhesive spheres (compare [12] with [30]) since at the corresponding compression during impact the surface energy due to the adhesion can be neglected compared with the elastic energy of the bulk. Consequently, the function $\varepsilon(v)$ has a maximum for moderate impact velocity.

For nanoparticles, the description by means of the coefficient of restitution is insufficient due to lack of homogeneity. Instead, the crystalline structure of the bulk material leads to a pronounced dependence of the rebound behavior on the angular orientation of the particles at the instant of the collision. Nevertheless, if we average the rebound velocity over the orientation, we obtain a similar behavior of the averaged coefficient of restitution as for the case of adhesive viscoelastic spheres, for the same reasons as discussed above.

In the current paper, we present a description of the impact behavior of nanoparticles beyond the description through an averaged coefficient of restitution. That is, we investigated the collision of a fcc crystalline nanoparticle with a crystalline wall with emphasis on the influence of the angular orientation of the particle at the instant of impact. We considered the main observables, that is, the degree of plastic deformation characterized by the perturbation of the lattice structure upon impact, the maximal interaction force during the process of impact, the coefficient of normal restitution, and the sticking probability. While all of these quantities reveal very large fluctuations when averaged naïvely, we show that the scatter is reduced largely when averaging by means of a variable, Ω, describing the angular orientation. Thus, orientations

characterized by similar values of Ω lead to similar mechanical characteristics such as plastic deformation, interaction force, coefficient of restitution, and sticking probability. Therefore, we conclude that the orientation of the particle prior to impact may be well characterized by the here introduced calculus Ω and its probability measure P_Ω. Consequently, we conclude that Ω is a suitable measure to characterize impact properties. In particular, we come to the following results.

(1) In the meta size range from about 2.5 to 7.5 nm, there exists no large bulk phase inside of the particle, the pressing upon impact is quite low, and thus the change of the shear angles is quite low. This is the reason why we observe anisotropy effects that could not be observed for particles with a size above about 10 nm. For even smaller particles than 2.5 nm, the surface forces completely dominate the volume forces and thus the required shear stress for plane gliding is not easily obtained. It is this delicate interplay between surface and volume forces that arises from the particle size that is responsible for the observed orientation-dependent effects, not the material itself. So the results should generalize to any material that is not too soft.

(2) The analysis of numerical molecular dynamics simulation of the impact properties as functions, $f(v_\mathrm{i}, P_\Omega)$ (where f stands for the above-mentioned characteristics), of the impact velocity, v_i, and the angular orientation characterized by Ω, reveals a rich phenomenology of orientation-dependent effects. By means of Ω and P_Ω we are able to explain these effects in full detail.

(3) Describing the system by v_i and Ω, we obtain quantitative results for the parameter space corresponding to certain characteristic behavior and identify regions of orientations with clearly distinct behavior for all observables considered.

(4) We identified a yet unknown high-velocity effect at $v_\mathrm{i} \approx 300\,\mathrm{m/s}$ for 15% of all orientations arising from a sophisticated interplay of impact energy and multiplane gliding. With increasing impact velocity, this effect deteriorates and the behavior becomes independent of the particle's orientation.

(5) By comparison of the standard deviations of $F_\mathrm{max}(v_i, P_\Omega)$ and $e_\mathrm{n}(v_i, P_\Omega)$ with $F_\mathrm{max}(v_i, P_\mathrm{SF})$ and $e_\mathrm{n}(v_i, P_\mathrm{SF})$ we argue that the orientation-dependent impact properties are more significantly characterized by means of P_Ω than P_SF. Therefore, we believe that Ω, which has a direct and intuitive relation to the geometric arrangement of the fcc planes prior to the impact, is better suited as a quantitative measure than the maximal Schmid factor to characterize the orientation-dependent impact mechanics.

In the present paper, we consider the orientation dependence of the impact properties for a specific set of material parameters. An exhaustive study of the dependence on material properties is not feasible due to enormous computer time requirements. Nevertheless, we believe that the results and the corresponding explanations apply for a certain range of material parameters and, more important, particle size, d. For very small particles ($d \lesssim 2.5$ nm) the behavior is fully dominated by surface effects, thus volume effects such as plane gliding are suppressed. In contrast, for larger particles ($d \gtrsim 7.5$ nm), the deformation of the impacting particle is restricted to a small volume close to the contact region. In the bulk of the particle, the required shear stress for plane gliding is not achieved and, thus, the crystalline structure of the particle would not lead to a significant orientation dependence. Therefore, we conclude that the size of the particles and the corresponding relation of surface and volume forces are more relevant for the orientation-dependent behavior of the impact rather than the pure material properties entering the atom-atom interaction force via Eqs. (1) and (2).

ACKNOWLEDGMENTS

We thank the German Research Foundation (Deutsche Forschungsgemeinschaft) for funding through the Cluster of Excellence "Engineering of Advanced Materials," the Collaborative Research Center SFB814, and Grant No. PO472/20-2. We gratefully acknowledge the computing time granted by the John von Neumann Institute for Computing and provided on the supercomputer JUROPA at Jülich Supercomputing Centre.

[1] G. Gilardi and I. Sharf, Literature survey of contact dynamics modelling, Mech. Mach. Theory **37**, 1213 (2002).

[2] D. Guo, G. Xie, and J. Luo, Mechanical properties of nanoparticles: Basics and applications, J. Phys. D **47**, 013001 (2014).

[3] H. Hertz, Ueber die Berührung fester elastischer Körper, J. für die Reine Angew. Math. **92**, 156 (1882).

[4] N. V. Brilliantov, F. Spahn, J.-M. Hertzsch, and T. Pöschel, Model for collisions in granular gases, Phys. Rev. E **53**, 5382 (1996).

[5] K. L. Johnson, K. Kendall, and A. D. Roberts, Surface energy and the contact of elastic solids, Proc. R. Soc. A **324**, 301 (1971).

[6] E. Barthel, Adhesive elastic contacts: JKR and more, J. Phys. D **41**, 163001 (2008).

[7] P. Armstrong and W. Peukert, Size effects in the elastic deformation behavior of metallic nanoparticles, J. Nanopart. Res. **14**, 1288 (2012).

[8] T. Schwager and T. Pöschel, Coefficient of restitution for viscoelastic spheres: The effect of delayed recovery, Phys. Rev. E **78**, 051304 (2008).

[9] T. Schwager and T. Pöschel, Coefficient of normal restitution of viscous particles and cooling rate of granular gases, Phys. Rev. E **57**, 650 (1998).

[10] M. Gensch and A. P. Weber, Rebound behavior of nanoparticle-agglomerates, Adv. Powder Technol. **28**, 1930 (2017).

[11] H. Kuninaka and H. Hayakawa, Simulation of cohesive head-on collisions of thermally activated nanoclusters, Phys. Rev. E **79**, 031309 (2009).

[12] N. V. Brilliantov, N. Albers, F. Spahn, and T. Pöschel, Collision dynamics of granular particles with adhesion, Phys. Rev. E **76**, 051302 (2007).

[13] S. Jung, D. Suh, and W. Yoon, Molecular dynamics simulation on the energy exchanges and adhesion probability of a nano-sized particle colliding with a weakly attractive static surface, J. Aerosol Sci. **41**, 745 (2010).

[14] L. B. Han, Q. An, S. N. Luo, and W. A. Goddard III, Ultra-elastic and inelastic impact of Cu nanoparticles, Mater. Lett. **64**, 2230 (2010).

[15] Y. Takato, S. Sen, and J. B. Lechman, Strong plastic deformation and softening of fast colliding nanoparticles, Phys. Rev. E **89**, 033308 (2014).

[16] E. Schmid and W. Boas, *Plasticity of Crystals* (Hughes, London, 1950).

[17] A. Awasthi and S. C. Hendy, Dependence of adhesion and reflection on orientation in nanocluster deposition, Adv. Sci. Tech. **51**, 127 (2006).

[18] E. N. Millán, D. R. Tramontina, H. M. Urbassek, and E. M. Bringa, The elastic-plastic transition in nanoparticle collisions, Phys. Chem. Chem. Phys. **18**, 3423 (2016).

[19] E. N. Millán, D. R. Tramontina, H. M. Urbassek, and E. M. Bringa, Nucleation of plasticity in nanoparticle collisions, Phys. Rev. E **93**, 063004 (2016).

[20] C. Schöner, S. Rennecke, A. P. Weber, and T. Pöschel, Introduction of a new technique to measure the coefficient of restitution for nanoparticles, Chemie Ingenieur Technik **86**, 365 (2014).

[21] M. S. Daw, S. M. Foiles, and M. I. Baskes, The embedded-atom method: A review of theory and applications, Mater. Sci. Rep. **9**, 251 (1993).

[22] S. M. Foiles, M. I. Baskes, and M. S. Daw, Embedded-atom-method functions for the fcc metals Cu, Ag, Au, Ni, Pd, Pt, and their alloys, Phys. Rev. B **33**, 7983 (1986).

[23] T. Halicioglu and G. M. Pound, Calculation of potential energy parameters form crystalline state properties, Phys. Status Solidi A **30**, 619 (1975).

[24] S. Plimpton, Fast parallel algorithms for short-range molecular dynamics, J. Comput. Phys. **117**, 1 (1995).

[25] R. E. Miles, On random rotations in R^3, Biometrika **52**, 636 (1965).

[26] G. Marsaglia, Choosing a point from the surface of a sphere, Ann. Math. Statist. **43**, 645 (1972).

[27] R. Ramírez, T. Pöschel, N. V. Brilliantov, and T. Schwager, Coefficient of restitution of colliding viscoelastic spheres, Phys. Rev. E **60**, 4465 (1999).

[28] T. Schwager, Coefficient of restitution for viscoelastic disks, Phys. Rev. E **75**, 051305 (2007).

[29] T. Schwager and T. Pöschel, Coefficient of restitution and linear-dashpot model revisited, Granular Matter **9**, 465 (2007).

[30] N. V. Brilliantov, N. Albers, F. Spahn, and T. Pöschel, Collision dynamics of granular particles with adhesion, Phys. Rev. E **87**, 039904(E) (2013).